# Cu(In,Ga)Se2 based ultrathin solar cells: the pathway from lab rigid to large scale flexible technology

**Tomás Lopes** ( tomas.lopes@inl.int )
INL- International Iberian Nanotechnology laboratory https://orcid.org/0000-0002-1266-386X

**Jennifer Teixeira**
INL- International Iberian Nanotechnology laboratory

**Marco Curado**
INL- International Iberian Nanotechnology laboratory

**Bernado Ferreira**
INL- International Iberian Nanotechnology laboratory

**Antonio Oliveira**
INL- International Iberian Nanotechnology laboratory

**José Cunha**
INL- International Iberian Nanotechnology laboratory

**Margarida Monteiro**
INL- International Iberian Nanotechnology laboratory

**André Violas**
INL- International Iberian Nanotechnology laboratory

**João Barbosa**
INL- International Iberian Nanotechnology laboratory

**Patricia Sousa**
INL- International Iberian Nanotechnology laboratory

**Ihsan Çaha**
INL- International Iberian Nanotechnology laboratory https://orcid.org/0000-0002-8212-874X

**Jérôme Borme**
INL- International Iberian Nanotechnology laboratory

**Kevin Oliveira**
INL- International Iberian Nanotechnology laboratory

**Johan Ring**
Obducat AB

**Wei Chen**
Uppsala University

**Ye Zhou**

Obducat AB
**Klara Takei**
Midsummer AB
**Esko Niemi**
Midsummer AB
**Leonard Francis**
INL- International Iberian Nanotechnology laboratory
**Marika Edoff**
Upsalla University
**Guy Brammertz**
Energyville 2
**Paulo Fernandes**
INL- International Iberian Nanotechnology laboratory
**Bart Vermang**
IMEC-IMOMEC
**Pedro Salomé**
INL- International Iberian Nanotechnology laboratory

**Article**

**Keywords:**

**Posted Date:** August 26th, 2022

**DOI:** https://doi.org/10.21203/rs.3.rs-1957042/v1

# Cu(In,Ga)$Se_2$ based ultrathin solar cells: the pathway from lab rigid to large scale flexible technology

T.S. Lopes [*1,2,3,4], J.P. Teixeira[*1], M.A. Curado[1,5], B.R. Ferreira[1], A.J.N. Oliveira[1,6,7], J.M.V. Cunha[1,6,7], M. Monteiro[1], A. Violas,[1,6,7], J.R.S. Barbosa[1], P.C. Sousa[1], I. Çaha[1], J. Borme[1], K. Oliveira[1], J. Ring[8], W.C. Chen[9], Y. Zhou[8], K. Takei[10], E. Niemi[10], F.L. Deepak[1], M. Edoff[9], G. Brammertz[2,3,4], P.A. Fernandes[1,7,11], B. Vermang[2,3,4], P.M.P. Salomé[1,6]

Affiliations

1-INL – International Iberian Nanotechnology Laboratory, Avenida Mestre José Veiga, 4715-330 Braga, Portugal
2-Hasselt University, imo-imomec, Martelarenlaan 42, 3500 Hasselt, Belgium
3-Imec, imo-imomec, Thor Park 8320, 3600 Genk, Belgium
4-EnergyVille, imo-imec, ThorPark 8320, 3600 Genk, Belgium
5-CFisUC, Department of Physics, University of Coimbra, P-3004-516 Coimbra, Portugal
6-Departamento de Física, Universidade de Aveiro, Campus Universitário de Santiago, 3810-193 Aveiro, Portugal
7-i3N, Universidade de Aveiro, Campus Universitário de Santiago, 3810-193 Aveiro, Portugal
8-Obducat AB, Medicon Village, 223 63 Lund Sweden
9-Ångström Laboratory, Department of Engineering Sciences, Uppsala University, 751 21 Uppsala, Sweden
10-Midsummer AB, Elektronikhöjden 6,SE-17543 Järfälla, Sweden
11-CIETI, Departamento de Física, Instituto Superior de Engenharia do Porto, Instituto Politécnico do Porto, 4200-072, Porto Portugal

* Corresponding authors: tomas.lopes@inl.int; jennifer.teixeira@inl.int

## Abstract

For the first time, the incorporation of interface passivation structures in ultrathin Cu(In,Ga)$Se_2$ (CIGS) based solar cells is shown in a flexible lightweight stainless-steel substrate. The fabrication was based on an industry scalable lithography technique - nanoimprint lithography (NIL) - for a 15x15 $cm^2$ dielectric layer patterning, needed to reduce optoelectronic losses at the rear interface. The nanopatterning schemes are usually developed by lithographic techniques or by processes with limited scalability and reproducibility (nanoparticle lift-off, spin-coating, etc). However, in this work the dielectric layer is patterned using NIL, a low cost, large area, high resolution, and high throughput technique. To assess the NIL performance, devices with a NIL nanopatterned dielectric layer are benchmarked against electron-beam lithography (EBL) patterning, using rigid substrates. Up to now, EBL is considered the most reliable technique for patterning laboratory samples. The device patterned by NIL shows similar light to power conversion efficiency average values compared to the EBL patterned device - 12.6 % vs 12.3 %, respectively - highlighting the NIL potential for application in the solar cell sector. Moreover, the impact of the lithographic processes, such as different etch by-products, in the rigid solar cells' figures of merit were evaluated from an elemental point of view via X-ray Photoelectron Spectroscopy and electrically through a Solar Cell Capacitance Simulator (SCAPS) fitting procedure. After an optimised NIL process, the device on stainless-steel achieved an average power conversion efficiency value of 11.7 % - a slightly lower value than the one obtained for the rigid approach, due to additional challenges raised by processing and handling steel substrates, even though scanning transmission electron microscopy did not show any clear evidence of impurity diffusion towards the absorber. Notwithstanding, time-resolved photoluminescence results strongly suggested the presence of additional non-radiative recombination mechanisms in the stainless-steel absorber, which were not detected in the rigid solar cells, and are compatible with elemental diffusion from the substrate. Nevertheless, bending tests on the stainless-steel device demonstrated the mechanical stability of the CIGS-based device up to 500 bending cycles.

# Introduction

Silicon (Si) wafer-based technology dominates the photovoltaic (PV) market share (≈92 %), while Cu(In,Ga)$Se_2$ (CIGS) has only a minor part, with 2 % [1]. Despite its low market share, CIGS PV shows lower manufacturing costs and material consumption over Si wafer technology, having the potential to be the cornerstone for building-integrated PV (BIPV), due to its applicability for lightweight and flexible applications [2,3].

Conventionally, CIGS solar cells are developed using soda-lime glass (SLG) as a substrate. However, SLG is a concern for scalability due to high fabrication costs during module assembly and it also increases the module weight[3]. Thus, efforts have been made to develop high-efficiency CIGS solar cells with different substrates, such as flexible substrates, that can replace the SLG, mitigating the final device's cost, weight and rigidity. However, the replacement of SLG is complex due to the panoply of requirements that the substrate must meet due to the CIGS composition and growth conditions: similar thermal expansion coefficient with CIGS, thermal stability at high temperatures (> 400°C), chemical inertness with CIGS elements, among others [4,5]. The prime candidates for flexible substrates are metals and polymers. Metals show high thermal stability but require an additional layer to block elemental diffusion. In contrast, for polymers, only polyimides can withstand temperatures higher than 400 °C, but the thermal expansion coefficient is not compatible with the CIGS one [5]. With these several requirements, breakthroughs in the CIGS technology are usually accomplished with an SLG substrate. Despite the challenges of replacing SLG, the performance of CIGS solar cells performances with flexible substrates are not far from those achieved by SLG ones, as CIGS solar cells on flexible substrates show an efficiency value of 21.4 %, with SLG reaching 23.35 %[6]. Furthermore, reducing the absorber thickness to the ultrathin range is required to fully exploit the solar cell device's flexibility. However, by thinning the absorber, recombination losses at the rear interface became a major loss mechanism. One strategy to tackle those losses is to passivate the rear interface by depositing a dielectric layer between the absorber and the rear electrode [7–12]. These passivation layers need to be patterned to establish electrical contact. The ideal contact dimensions need to be optimised, considering their geometry and spacing. Nonetheless, a high coverage area by the dielectric is preferred for an efficient passivation [13,14]. Electron-beam lithography (EBL) and optical lithography have successfully pattern dielectric layers in ultrathin CIGS solar cells [10,11,13,15]. While optical lithography offers high throughput, its drawback is its low resolution. Although EBL can pattern with high resolution, it suffers from high cost and low direct-write speed, hindering its scalability in the CIGS industry. To leverage the ultrathin CIGS technology, a patterning technique with low cost, high throughput, and high resolution is required. One potential candidate that matches such requirements is nanoimprint lithography (NIL). NIL acts as a parallel patterning method in which a surface pattern, a stamp, is replicated into a material-coated substrate by mechanical contact and 3D material displacement [16]. A significant amount of research has been done to explore the NIL capabilities and meet the industry demands since its suggestion by Stephen Cheng *et al.* [17]. As a result, NIL is already used in several technologies and industries, such as organic light emission displays, memories, biomedical devices, microelectronics, among others [18–25]. However, NIL is still to be established in the (ultra)thin film solar cell's technology.

In order to meet the need for on-site renewable energy, lightweight CIGS based solar cells in flexible substrates are explored in this study with rear passivation by NIL. We studied rigid devices with a $SiO_x$ passivation layer patterned by NIL and benchmarked them with devices patterned by EBL. After that, the scalability capabilities of NIL are demonstrated through the patterning of a 15x15 $cm^2$ semi-squared flexible stainless-steel substrate. Silver (Ag) was incorporated into the CIGS layer (ACIGS), as adding Ag improves crystallinity of thin CIGS devices and allows for low deposition temperatures, matching the requirements of the flexible substrate[26–28]. The flexible device shows a slightly lower

performance than the rigid ones. A set of advanced characterisation techniques was used to understand all the devices, their performance, and to design an experiment to obtain flexible solar cells with a comparable performance to their rigid counterparts. The solar cells' performance shows the potential for industry scalability for flexible and lightweight ultrathin CIGS based devices, and NIL is a suitable candidate to follow this upscale.

## Materials and Methods

Three ultrathin CIGS based devices were fabricated: two SLG-based and one with a flexible stainless-steel substrate. For the case of SLG-based substrates, two different patterning techniques were compared: one substrate was patterned by EBL (EBL-SLG) and the other one by NIL (). Afterwards, a 15x15 $cm^2$ flexible stainless-steel substrate was patterned using a NIL process (Flexible). Table 1 summarizes the fabricated devices with the description of the fabricated substrates. Given the dimensions of the stainless-steel substrate, a NIL stamp able of patterning such large area was developed. $SiO_x$ passivation layers with 8 and 20 nm were deposited on a Mo contact for the steel and in the SLG based substrates, respectively, through plasma-enhanced chemical vapour deposition (PECVD) in an SPTS MPX CVD system[29–31].A thinner $SiO_x$ for the Flexible sample was chosen, since a lower thickness is more suitable for flexible applications[32]. The $SiO_x$ layer thickness was estimated by an OPM NanoCalc optical profilometry system.

Table 1 – Description of the samples' nomenclature, the thickness of the passivation layer, lithography used and the rear stack.

| Substrate/Device name | Lithography technique | Rear stack |
|---|---|---|
| EBL-SLG | EBL | SLG/Mo/$SiO_x$ |
| NIL-SLG | NIL | SLG/Mo/$SiO_x$ |
| Flexible | NIL | Steel/Mo/$SiO_x$ |

### SLG based substrates lithography

Figure 1 shows a schematic of the lithography process for the SLG-based substrates coated with $SiO_x$. We used the same pattern architecture for both substrates for comparison purposes: 100 nm point contacts diameter with 1 µm pitch in a hexagonal array. The pattern dimensions were chosen to balance a high dielectric coverage area with a low EBL exposure time[13]. The EBL procedure started with spin-coating an electron sensitive resist, 430 nm of Polymethyl methacrylate (PMMA) (Figure 1b)), followed by an exposure step (Figure 1c.2)) using an acceleration voltage of 100 kV in a Vistec 5200 system. Then, the pattern was developed for 40 s using a Methyl isobutyl ketone (MIBK) developer diluted in Isopropanol (IPA). Afterwards, the exposed $SiO_x$ layer was opened by Reactive Ion Etching (RIE) (Figure 1e)) in an STPS Advanced Plasma System (APS) at 13.6 MHz in $C_4F_8$ chemistry for 45 s. Finally, the remaining PMMA was removed (Figure 1f)) by immersing the substrate in an ultrasound bath in acetone. For the NIL patterned substrate, the process started by spin-coating a Simultaneous Thermal and UV (STU®) resist (TU7-120, Obducat) with a thickness of 150 nm (Figure 1b)). Before the imprint, the hexagonal array contact pattern was transferred from a 100 mm nickel stamp to an Intermediate Polymer Stamp (IPS ®) by UV-NIL. The use of IPS® extends the initial stamp lifetime and enables to work with UV for non-transparent substrates and moderate pressures [33,34]. A UV-NIL process was conducted to transfer the pattern to the IPS®, in a NanoImprint Eitre 6 system (Obducat AB). Initially, the pressure was raised to 15 bar for 30 s, followed by UV exposure for 180 s, while maintaining the pressure. Subsequently, the IPS® was rolled to the substrate for the imprint. The imprint started with increasing the stage temperature to 65 °C with a pressure of 15 bar for 80 s.

Then the UV light was turned on for 180 s, while maintaining the temperature and pressure (Figure 1c.1)). A 70 nm residual TU7-120 resist layer was removed by $O_2$ etch in an STPS Pegasus system for 5 s with an $O_2$ flow of 115 sccm at 13.56 MHz (Figure 1d.1)). Then, RIE was used to open the point contacts in an STPS Inductively Coupled Plasma Source (ICP) system for 50 s in a $BCl_3$ chemistry at 13.56 MHz (Figure 1e)). The resist layer was stripped by $O_2$ plasma ashing with an $O_2$ and Ar flow of 200 sccm and 20 sccm, respectively (Figure 1f)).

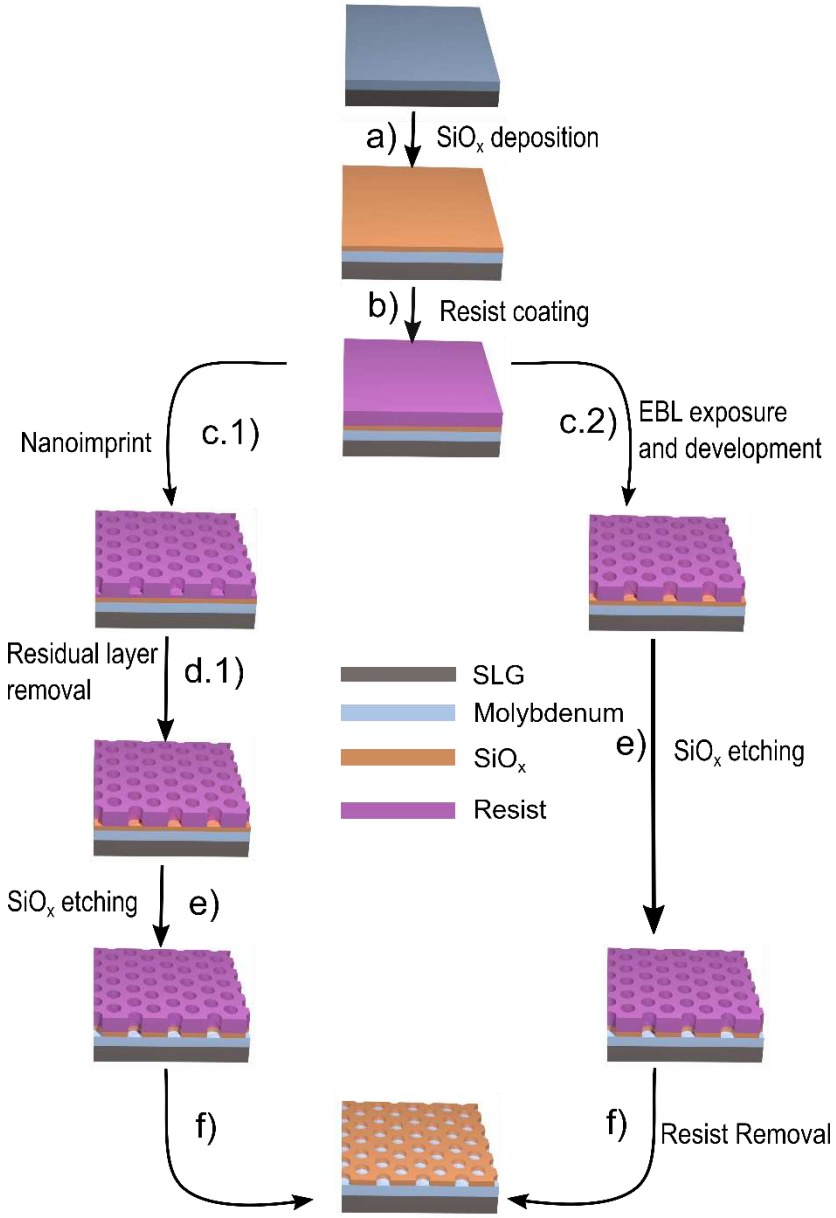


Figure 1 - Schematic representation of the lithography processes for patterning SLG based substrates with NIL (left) and EBL (right). Not at scale.

## Flexible Stainless-steel substrate lithography

### 200 mm point contact Si stamp fabrication

The fabrication of a 200 mm Si stamp with point contacts was divided into two lithographic processes: i) EBL, to produce 400 nm wide nano-pillars, with the same EBL procedure as described elsewhere[35]; and ii) NIL, to invert the stamp polarity from pillars to point contacts. Figure 2 shows a schematic of the workflow for a two-step polarity inversion process to manufacture a 200 mm point contact Si

stamp from a Si pillar stamp. This workflow requires two polarity inversion processes, which involves two distinct working stamps, namely an Ormostamp polymer (Micro-Resist Technology GmbH) and an IPS®, which results in a point contact and a pillar pattern, respectively.

The first polarity inversion was conducted by dispensing an Ormostamp droplet on a Si pillar stamp, placing a glass wafer on top of the Ormostamp and squeezing it for a uniform distribution at 5 bar for 300 s, followed by UV exposure for 35 s, obtaining a point contact structure in this intermediate stamp (Figure 2a)). After the transfer process, 70 nm of an anti-sticking layer was deposited on the Ormostamp surface in an STPS Pegasus system for 10 s with 13.56 MHz in a $C_4F_8$ chemistry. For the second polarity inversion an IPS® was rolled into the Ormostamp surface, followed by a UV-NIL step. For this process, the pressure was raised to 15 bar for 30 s with no UV, followed by UV exposure for 180 s while maintaining the pressure, obtaining a pillar structure on the IPS® (Figure 2b)). The fabrication process of the Si point contact stamp was then performed through a STU-NIL process using the IPS® pillar intermediate stamp. For that, the IPS® was rolled on a Si wafer coated with 500 nm of TU7- 310 Obducat resist. In the STU-NIL step, the temperature and pressure were raised to 65 °C and 15 bar and maintained for 80 s, followed by UV exposure for 180 s, while maintaining the above conditions (Figure 2c)). The resulting residual layer was 100 nm and was removed with an 8 s $O_2$ etching process in an STPS Pegasus system (Figure 2d)) and followed by an etch of the Si layer by 110 nm in an STPS ICP system (Figure 2e)). At the end of the etching process, the remaining resist was stripped with $O_2$ plasma ashing (Figure 2f)).

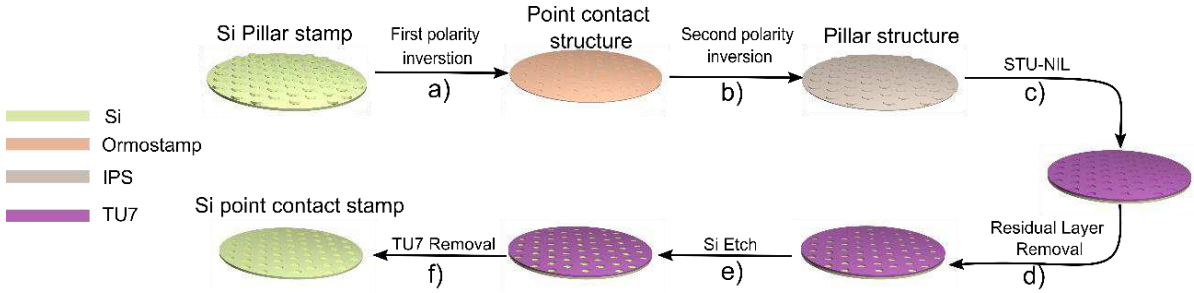


Figure 2 - Schematic with the 200 mm point contact Si Stamp fabrication steps. Not at scale.

## NIL process for the flexible steel substrates

The lithography process for the flexible stainless-steel substrate, with a hexagonal array of 400 nm point contacts with a pitch of 2 µm follows the NIL procedure shown in Figure 1. We used the Si stamp described above for the stainless-steel substrate imprinting. For the lithography process, the wafer was coated with 160 nm of TU7-120 resist (Figure 1b)). Before the imprint, the pattern in the Si stamp was transferred to an IPS®, by UV-NIL for 180 s at 10 bar, the Si stamp was coated with an anti-sticking layer to ease the demoulding in an STPS Pegasus system. After the transfer, an anti-sticking layer was deposited on the IPS® surface in an STPS Pegasus system. The imprint conditions were done with the same parameters as the SLG-based substrate (Figure 1c.1)). The resist residual layer was removed with an $O_2$ etch in an SPTS Pegasus system for 5 s with an $O_2$ flow of 115 sccm (Figure 1d.1)). Afterwards, RIE was used to open the point contacts in an SPTS APS for 20 s (Figure 1e)). The remaining resist layer was removed through an $O_2$ plasma ashing (Figure 1f)).

### Solar cell integration

After the lithography processes, all the substrates from both sets were integrated into ultrathin ACIGS based solar cells. Before the ACIGS growth, a 15 nm Sodium fluoride (NaF) was evaporated on all substrates. The ACIGS was grown in a one-stage co-evaporation process. For the SLG glass substrates, the estimated ACIGS thickness was 720 nm with ([Ag]+[Cu])/([Ga]+[In]) ≈ 0.82, [Ga]/([Ga]+[In]) ≈ 0.40, and [Ag]/([Ag]+[Cu]) ≈ 0.09. For the flexible stainless-steel substrate the ACIGS layer had an estimated thickness of 650 nm, with [Ag]+[Cu]/([Ga]+[In]) ≈ 0.88, [Ga]/([Ga]+[In]) ≈ 0.43, and [Ag]/([Ag]+[Cu]) ≈ 0.12, as determined by X-ray fluorescence (XRF) performed in a Panalytical Epsilon 5. After the growth of the ACIGS layer, the remaining CdS/i-ZnO/ZnO:Al layers were fabricated following the Ångstrom baseline standard process[36]. Per device, 12 solar cells with an area of 0.1 $cm^2$ were individualised by a lithography process.

### Substrates and Solar cells characterisation

Scanning Electron Microscopy (SEM) was used for top view images of the substrates with acceleration voltages of 3 kV and 5 kV in a NovaNanoSEM 650 FEI system. Before the ACIGS growth, the substrates' architectures were analysed, by a Bruker Icon Atomic Microscope (AFM) in tapping mode with a scan rate of 0.5 Hz. Completed solar cells were characterised by current-density against voltage (J-V) measurements with an AM1.5 G illumination source at 1000 $W.m^{-2}$, performed in a home-built system. Bending cycles were conducted manually in a tube with a 14.4 mm radius. In total, 500 bends were performed, and illuminated J-V measurements were conducted before bending and after 1, 5, 10, 20, 50, 100, and 500 bending cycles, after returning the device to a planar state. An ESCALAB™ 250Xi (Thermo Scientific™) XPS system was used for the substrate surface survey measurement, with an X-ray monochromatic source of Al $K_\alpha$ (1486.86 eV). The measurements conditions were used with a pass energy of 200eV and, a dwell time of 300 ms, three repetitions, and a scan region between 0 eV and 1200 eV was carried out. Scanning Transmission Electron Microscopy (STEM) with energy-dispersive X-ray spectroscopy (EDS) was conducted on the Flexible device in a probe-corrected FEI Titan G2 ChemiSTEM equipped with a Super-X EDX System, operating at 200 kV. The device lamella was prepared by focused ion beam (FIB) preparation in a FEI Dual-Beam Helios 450S. For the EDS maps, the following elements and their corresponding characteristic emission spectrum lines were chosen: Fe $K_\alpha$=6.403 keV, Cr $K_\alpha$= 5.414 keV, Ni $K_\alpha$=7.477 keV, Ti $K_\alpha$=4.508 keV, Si $K_\alpha$=1.740 keV, Mo $K_\alpha$=17.441 eV, Ag $L_\alpha$=3.150 keV, Cu $K_\alpha$=8.040 keV, Ga $K_\alpha$=9.241 keV, In $L_\alpha$ = 24.210 keV, and Se $K_\alpha$=11.207 keV. Time-Resolved Photoluminescence (TRPL) was measured at room temperature with a Picoquant photospectrometer with a TimeHarp 260 single photon counter. The excitation intensity was approximately 0.1 $W.cm^{-2}$ and the frequency was 3 MHz with an excitation wavelength of 532 nm. The one dimensional SCAPS was used following Violas *et al.* baseline[37] to fit the experimental J-V curves allowing for an in-depth discussion of the obtained electrical performance of the produced devices.

## Results and discussion

### Patterned substrates characterisation

Top view SEM images and cross-section AFM profiles were taken from the NIL-SLG and EBL-SLG substrates to determine the dimensions and profiles of the point contacts. Figure 3 a) and b) show top view SEM images of the NIL-SLG and EBL-SLG substrates, respectively. The average and standard deviation diameter value of 40 point contacts, per substrate, obtained through the SEM top view image analysis is 142 ± 9 nm for NIL-SLG and 129 ± 6 nm for EBL-SLG. The larger diameter for NIL-SLG likely arises from the $O_2$ etch process to remove the residual layer, which may enlarge the point contact dimension, due to its isotropic component. On the other hand, EBL-SLG substrate presents point contacts in an elliptical shape caused by astigmatism of the EBL system[15]. AFM cross-section

profiles of a representative point contact for NIL-SLG and EBL-SLG are shown in Figure 3 c) and d), respectively, with the 20 nm $SiO_x$ layer defined between the dashed lines. The AFM cross-section profiles show a complete etch of the $SiO_x$ layer for both substrates and even a minor etch of the Mo layer, ensuring the quasi-ohmic contact between the ACIGS and the Mo layer[30]. From the AFM cross-section profile, the point contact diameter average and standard deviation value for NIL-SLG is 47 ± 20 nm and 42 ± 16 nm for EBL-SLG. We should note that the difference between the diameter values obtained through top-view SEM images and the AFM profile comes from the etching steps that narrow the point contact into a "V" shape, as the SEM values comes from the top of the contact and the AFM ones are related with the effective interface diameter with the Mo. Nonetheless, the point contacts show similar dimensions for both lithography processes, which is desired since we aimed to have similar architectures, including equivalent over-etching results to minimise the morphological difference between substrates.

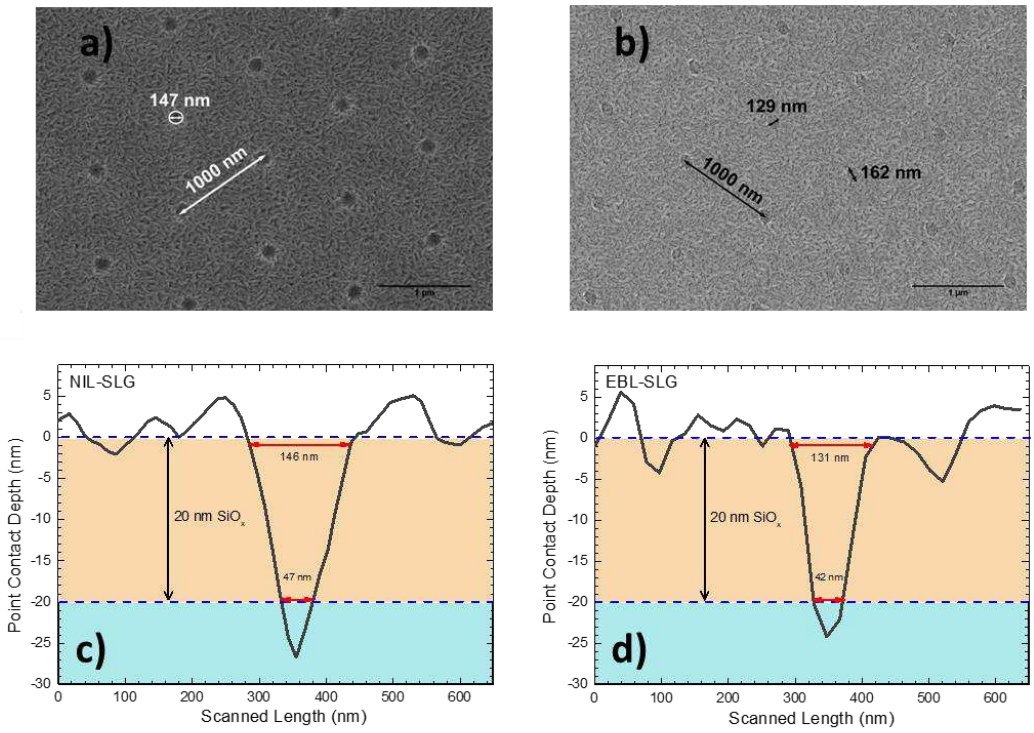


Figure 3 - Top-view SEM images of: a) NIL-SLG and b) EBL-SLG substrates. The SEM images were taken with a Horizon field width (HFW) of 5 µm and an acceleration voltage of 5 kV. AFM cross-section profiles of a representative point contact of: c) NIL-SLG and d) EBL-SLG substrates obtained with a scan rate of 0.5 Hz. We note that the AFM obtained distance for both substrates is within average values for the SEM measurements.

The 200 mm Si point contact stamp SEM top view images shown in Figure 4, were taken during the NIL fabrication to evaluate the process uniformity: i) the nanoimprinting process - Figure 4a.1) and a.2); ii) the residual layer removal - Figure 4b) and; iii) the resist removal - Figure 4c). Figure 4 a.1) and a.2) were taken at opposite edges of the wafer, with a distance of 40 mm, to access the demoulding quality. An imperfect demoulding process leads to elongation in a particular direction[34]. Figure 4 a.1) and a.2) show clearly defined circular point contacts, with no deformation, and an average dimension of 420 ± 12 nm. From the AFM profile presented in Figure 4d), the point contact seems to have well defined vertical sidewalls with a depth of 110 nm and a diameter of 405 nm, compatible with the SEM top view dimension. These results support the uniformity of employing NIL to perform a double

polarity inversion in the 200 mm fabricated stamp, and the high quality of the produced stamp to pattern the large scale solar cell.

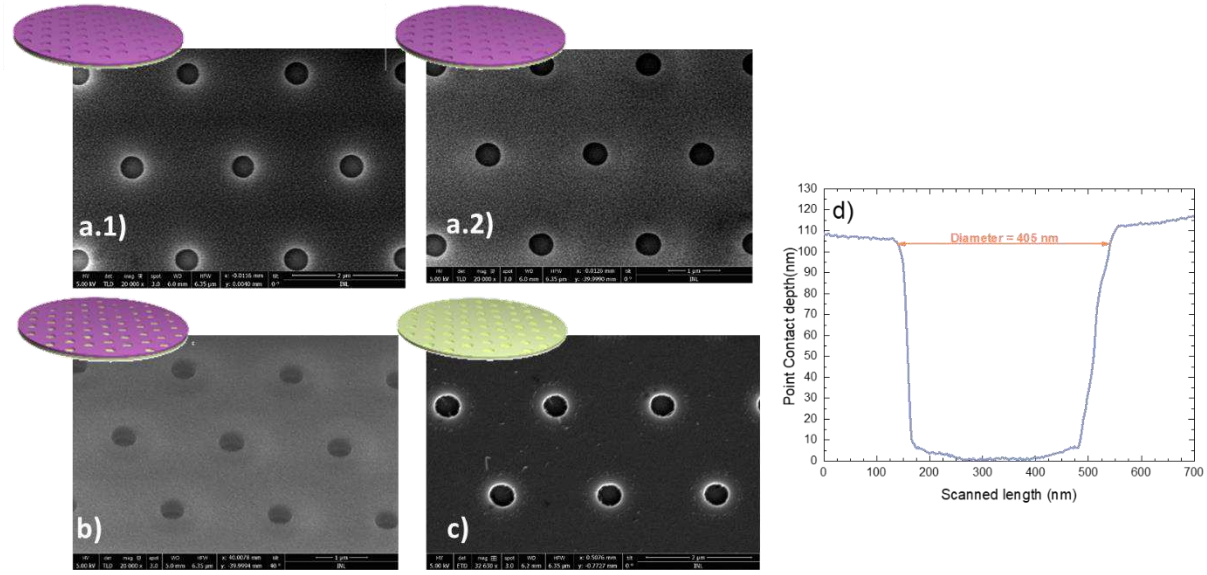


Figure 4 - Top view SEM images of the 200 mm point contact stamp a) after the NIL process, b) after the Si etching, and c) After the resist removal and wafer cleaning. d) AFM cross-section profile of one point contact of the Si stamp.

The patterning process of the Flexible highlights the industrialisation aspect of NIL, as the imprinting step took only 7 min. However, exposing the same pattern with EBL would take up to 8000 min of non-interrupted machine runtime. NIL on non-flat surface substrates, such as steel, commonly employs high pressure to overcome the surface roughness[16], hence SEM top-view images are mandatory to check the uniformity of the process[16]. Figure 5 shows the top-view SEM images of Flexible at opposite sites on the substrate after the resist removal process. From the top view SEM images, the point contacts show well-defined and circular dimensions, indicating a successful demoulding. An uniformity in shape geometry in the whole sample is important as demoulding can lead to artefacts in the shape of the features, as that is not the case here, we can conclude that the demoulding has no issues. The average diameter for the point contacts obtained by SEM images is 391 ± 39 nm. The uniformity of the point contacts shape indicates that our STU-NIL process and the use of a flexible IPS® can overcome the surface roughness of the steel wafer, leading to uniform features.

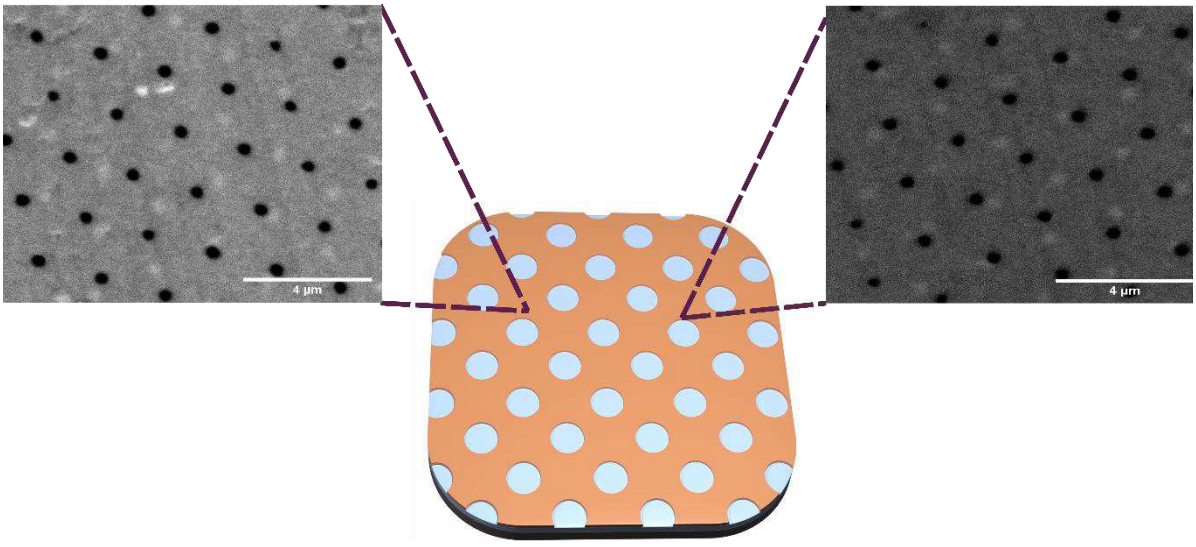

Figure 5 - Top view SEM images after the resist removal, at opposite sides of flexible substrate, with the identification on the location of the SEM images. The point contact shape and dimension are retained regardless of the distance between the measurement, which indicates high quality for the demoulding step.

## Solar cells results

The three studied devices' representative illuminated J-V curves and figures of merit average values are presented in Figure 6 a) and b), respectively. The average power conversion efficiency values obtained for SLG substrates are very close, 12.6 and 12.3 % for NIL-SLG and EBL-SLG devices, respectively. Nevertheless, a slight decreased value is obtained when moving to the large area flexible stainless-steel based device, 11.7 %, even though it is a less than 1 % conversion efficiency decrease. Such results highlight the potential of the developed process to include large flexible substrates in the CIGS based ultrathin solar cells portfolio[11,29,38,39]. The EBL-SLG device shows a roll-over behaviour, responsible for its FF value lower than NIL-SLG. This roll-over anomaly likely indicates a presence of an electronic barrier[40,41], which might be related with Na distribution problems[40,42]. Nonetheless, in the NIL-SLG device – which has the same pattern and received the same amount of NaF precursor - the said rollover isabsent. Remarkably, the NIL-SLG device achieved a FF value of 79.2 %, which is higher than the FF values obtained in high efficiency sub-micrometre CIGS-based solar cell devices[43,44], albeit 1.2 % lower than the one achieved in the current world record CIGS based thin film solar cell[45]. Nonetheless, an absolute decrease of 12.4 % in the FF value is observed for the Flexible device when compared to the NIL-SLG. This loss might be explained by the high roughness present in the steel substrate and by the difficulty in cell definition. AFM measurements show a root mean square surface roughness of 18.6 nm for the stack Steel/Mo, approximately 300 % higher than the one obtained for the SLG/Mo which is 4.9 nm. Notwithstanding, we highlight the low standard deviation values (Figure 6b)) for the Flexible devices, indicating the high uniformity of the individual solar cells. The Flexible devices show the highest $J_{SC}$ values amongst the fabricated solar cells, which may come from light trapping effects due to the steel surface roughness, which will increase the optical path length inside the device, thus increasing the $J_{SC}$ value[38]. Relative diffuse reflectance measurements of Steel/Mo and SLG/Mo substrates are presented in Figure 6c). A broadband increase is observed for the stainless-steel substrate. However, the light trapping effect evaluated through the inclusion of the obtained surface roughness in the solar cells architecture via 3D finite-difference time-domain optical simulations[46], shows a lower $J_{SC}$ enhancement than the one measured. Thus, optical phenomena are insufficient to solely explain the difference between the $J_{SC}$ of the Flexible and the SLG based devices[47]. Considering the SLG devices, a difference on the $J_{SC}$ value of 2.3 mA/cm$^2$ was obtained, while keeping 98 % of the EBL-SLG $V_{OC}$ value, the NIL-SLG device presents an unexpected decrease in the $J_{SC}$. So far, the obtained results show two main differences between the SLG solar cells; a 2.3 mA/cm$^2$ $J_{SC}$ difference between them, and a roll-over anomaly in the EBL-SLG suggesting charge extraction problems. These differences are unexpected as the substrate architecture is nominally the same, as well as the upcoming layers and its processing, including the absorber. We relate this difference to two major points: a non-uniform distribution of the Na doping, although both samples have the same NaF thickness, and/or the effectiveness of the passivation layer (chemical and field-effect passivation effects). Both these points should have somehow a connection to the lithographic process and its operational conditions - exposure, resists, and more importantly the chemical nature of the etch process, which was different for the two SLG based substrates. As the two SLG lithographic procedures required different etch processes, which inevitably led to different by-products, XPS surveys were performed on Mo based samples: without any etch procedure (Mo_Ref), after a $C_4F_8$ based etch in the Mo_EBL, and finally a $BCl_3$ based etch in the Mo_NIL. All the XPS surveys spectra are presented in Figure 6d). A major difference stands out: the Mo_EBL spectrum shows a fluor (F) contribution. None of the other samples show the presence of F. The F appears as by-product of the $C_4F_8$ based etch used

in the EBL sample. Despite the existence of F on the Mo_EBL surface, overall, the three samples have very similar spectra. No detrimental impact is expected by the presence of F in the EBL-SLG sample, as every studied sample had a NaF treatment, and this element is commonly used both in alkali-precursors in post-deposition treatments[40]. Moreover, it is not expected that F had an impact in the observed barrier in the EBL-SLG device, since the roll-over behaviour was also previously observed in devices with substrates architectures obtained through $BCl_3$ etch[13]. Nonetheless, extra F could potentially affect the NaF dissociation and chemistry during the CIGS growth and the relation between Na, O, F and Se and Na diffusion is quite complex[48,49]. Moreover, SCAPS software was used to further discuss the SLG-based devices electrical parameters. The implementation of an 1D Poisson solver along with complex architectures that may not be totally described by the one-diode model, bring an additional complexity in the deconvolution and discussion of the electrical parameters. In order to better describe the developed architectures, the SCAPS model was fitted to the EBL-SLG and NIL-SLG measured J-V curves, as shown in Figure 6e), by varying the rear contact barrier (i.e. contact work function) and the surface recombination velocity (SRV) for electrons and holes, in order to achieve the lowest Chi-square sum value. The fitted figures of merit are presented in Figure 6b). This model was implemented for five scenarios of compensation varied from 17 to 67 % in the bulk region, where 1) the rear contact transport barrier height was varied from 0 to 0.3 eV since a roll-over effect was observed in the EBL J-V curve, and 2) the SRV for electrons and holes were varied from $10^4$ to $10^2$ cm/s, as the rear passivation effect on SRV observed experimentally typically varies within such range values[50,51]. An important result comes from the compensation level that better describes the J-V curves, which is 11 % (abs.) higher for the EBL-SLG comparing to the NIL-SLG. This result is compatible with a more efficient integration of Na in the NIL-SLG device, raising the point that having additional F in the substrate may difficult the NaF dissociation and consequently the incorporation of Na on the ACIGS. Additionally, it is known that the Na presence is a prerequisite as a catalyst to the $MoSe_2$ formation providing a quasi-ohmic contact[52], which might explain the higher simulated series resistance ($R_S$) value for the EBL-SLG device. No significant rear barrier height was obtained for both devices. Therefore, the charge accumulation responsible for the roll-over effect might be related to other phenomena. Note that, in the EBL-SLG solar cell the contact area is 20 % lower than the NIL-SLG one, in addition the hole (h-)SRV obtained value for this device suggests a higher hole density available to be extracted, which may lead to charge accumulation at the rear contact in the EBL-SLG solar cell. The fitted figures of merit show lower SRV values for the EBL-SLG in comparison to the one obtained for the NIL-SLG. The presence of F in the Mo layer may create an additional field effect, allowing for an improvement in the $J_{SC}$ value. Although, an improved rear interface passivation effect might be obtained by the presence of F, it also affects the NaF dissociation and the compensation values, and therefore the optoelectronic properties of the ACIGS, leading to similar $V_{OC}$ values between both devices. Furthermore, given that the Flexible device also went through an etching process based on $C_4F_8$ and given its high $J_{SC}$ values, it is possible that for this sample the presence of F in the Mo surface together with the higher diffuse reflectance may be responsible for its high $J_{SC}$. However, a detrimental impact in the optoelectronic properties of the ACIGS is expected, which will affect the $V_{OC}$ value. Nonetheless, the large $V_{OC}$ drop observed in the stainless-steel device might not be fully explained by this effect, as it was seen that in the SLG-based devices the $V_{OC}$ values are similar.

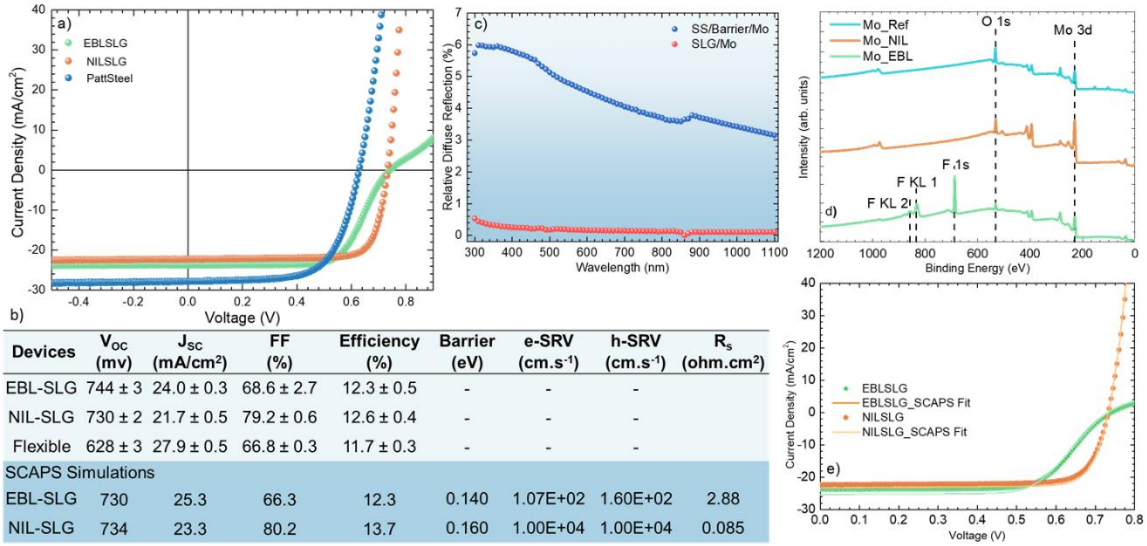


| Devices | $V_{OC}$ (mv) | $J_{SC}$ (mA/cm²) | FF (%) | Efficiency (%) | Barrier (eV) | e-SRV (cm.s⁻¹) | h-SRV (cm.s⁻¹) | $R_s$ (ohm.cm²) |
|---|---|---|---|---|---|---|---|---|
| EBL-SLG | 744 ± 3 | 24.0 ± 0.3 | 68.6 ± 2.7 | 12.3 ± 0.5 | - | - | - | |
| NIL-SLG | 730 ± 2 | 21.7 ± 0.5 | 79.2 ± 0.6 | 12.6 ± 0.4 | - | - | - | |
| Flexible | 628 ± 3 | 27.9 ± 0.5 | 66.8 ± 0.3 | 11.7 ± 0.3 | - | - | - | |
| SCAPS Simulations | | | | | | | | |
| EBL-SLG | 730 | 25.3 | 66.3 | 12.3 | 0.140 | 1.07E+02 | 1.60E+02 | 2.88 |
| NIL-SLG | 734 | 23.3 | 80.2 | 13.7 | 0.160 | 1.00E+04 | 1.00E+04 | 0.085 |

Figure 6 - a) Representative illuminated J-V curves; b) The figures of merit average and standard deviation values for the fabricated devices and in dark blue the ones obtained via SCAPS fit for EBL-SLG and NIL-SLG, additionally the rear barrier for holes, and the SRV for electrons and holes are also presented; c) Relative total diffuse reflection of Mo into a SLG and Stainless-steel substrate; d) XPS survey spectra of Mo based substrates without etch process, Mo_Ref, and with a $BCl_3$ and $C_4F_8$ based etch process for substrate Mo_NIL and Mo_EBL, respectively are shown; e) SCAPS fit to the EBL-SLG and NIL-SLG illuminated J-V curves presented in a).

It should be noted that the SLG based CIGS solar cells commonly show higher $V_{OC}$ values than those achieved by stainless-steel substrates[53,54], thus, the lower $V_{OC}$ value for Flexible solar cells is an expected but unwanted result. Common causes for such difference may come from diffusion of elements present in the steel substrate, such as iron (Fe), towards the CIGS[54,55], which might have occurred due to the used CIGS growth temperature[53]. The small drop in the overall Flexible performance is mostly due to the significant decrease in the $V_{OC}$ values. Thus, despite of the diffusion barrier and the $SiO_x$ passivation layer, some impurities may still diffuse towards the absorber. Thus, cross-section STEM images and EDS line scans were taken for the Flexible device to study the elemental distribution in the ACIGS layer. Figure 7a) shows a cross section STEM image for Flexible device, with Figure 7 b) and c) showing the EDS line scan profile for the substrate's elements throughout the complete device and the ACIGS elements plus Fe in the absorber layer, respectively. The STEM image shows a conformal layer growth of the solar cell stack layers. The complete device's line scan in Figure 7b) initially shows a high signal from elements present in the steel substrate, such as Fe and chromium (Cr), with Fe having the highest atomic percentage. A residual percentage of titanium (Ti) and nickel (Ni) was also detected into the stainless-steel substrate, while an increase in the atomic percentage of Ti was observed in the barrier region. The Si signal detected supports the $SiO_x$ based nature of that barrier. Moreover, once we reach the diffusion barrier, we observe a decrease of Fe and Cr elements, as Ni, Ti, and Cr reach a near zero atomic percentage at the Mo layer. Such a drop in atomic percentage indicates that the diffusion barrier together with Mo significantly prevented further diffusion of these elements onto the CIGS. Note that, at the Mo/ACIGS interface the Si signal increases. This phenomenon is explained due to the proximity between the Si $K_\alpha$=1.740 keV and the Se $L_\alpha$=1.379 keV, which indeed reflects the common formation of the nanometric $MoSe_2$ interfacial layer[30]. The elemental distribution in the ACIGS layer (Figure 7 c)) follows the trend expected for an inline deposition process. The Fe element was also scrutinized in this layer. However, only a very residual presence of Fe was detected, which does not allow for a clear conclusion considering its presence in the absorber, since it may be an artefact. In this regard, TRPL

measurements were performed in order to evaluate possible differences in the recombination mechanisms between devices. The TRPL decay of the three studied samples is presented in Figure 7d), being all well described by a biexponential function with two characteristic decay lifetimes[56–58]: $\tau_1$ is often linked to charge separation and $\tau_2$ to recombination mechanisms. A clear difference in the TRPL decay is observed between the SLG based devices and the stainless-steel one, which presents a faster decay in comparison to its SLG counterparts. Both SLG devices present similar decay curves, with slightly higher $\tau_1$ and $\tau_2$ values for the EBL-SLG in comparison to the NIL-SLG. The trend of the $\tau_2$ values from these two solar cells is well aligned with the one from the $V_{OC}$ values, both parameters showing a small gain for the EBL-SLG. Thus, no significant differences on the optoelectronic properties were found between the two SLG solar cells. Despite the many physical factors that may determine the TRPL decay, the significant change observed in the Flexible decay, strongly indicates additional non-radiative recombination mechanisms that are not present in the rigid devices, which is compatible with the low $V_{OC}$ value obtained for the Flexible solar cell. Therefore, elemental diffusion from the stainless-steel substrate at doping levels which are not detected by EDS might have diffused towards the ACIGS leading to additional non-radiative recombination channels, which might explain the much faster TRPL decay in the Flexible device in comparison to the rigid solar cells. Moving forward, the development of either new diffusion barriers and/or using a thicker Mo layer[54] should be developed to completely block metal diffusion towards the absorber, as it allows for a smoother transaction between laboratory devices and industry. Moreover, additional growth optimisation of CIGS based layers at low temperatures could also help to mitigate said issue[28,59] .

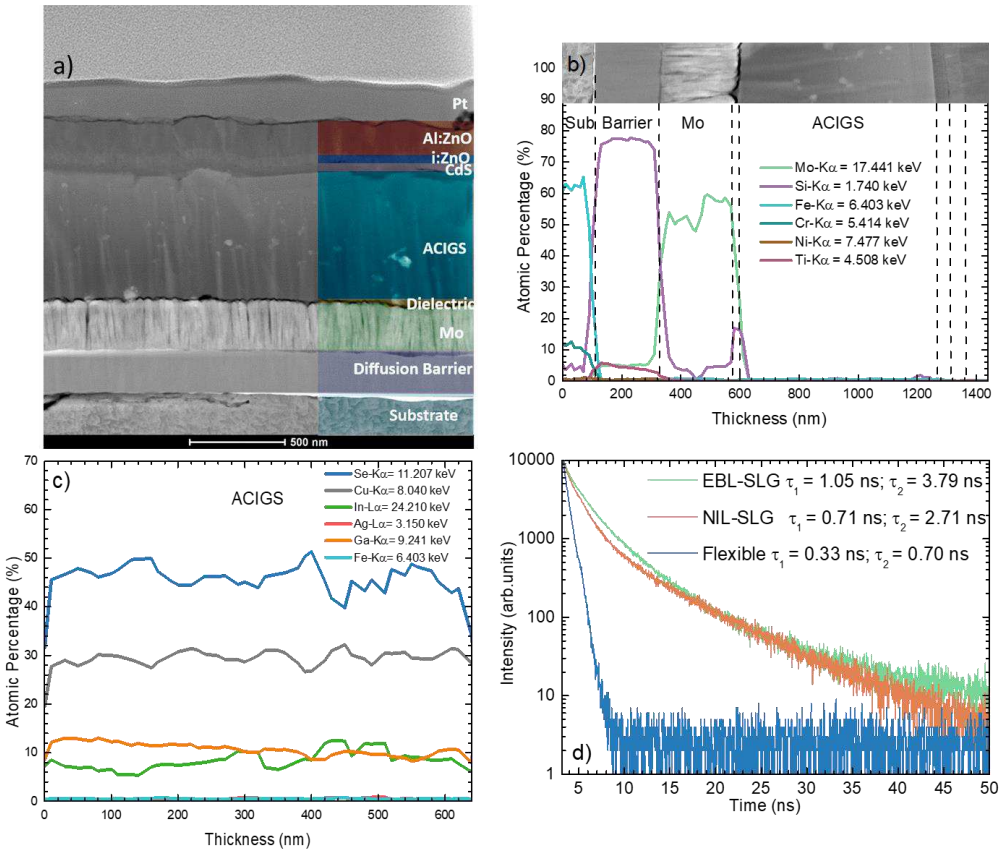


Figure 7 a) Cross section STEM image for Flexible device with the corresponding layers of the device identified; b) EDS line scan for the complete device. For clarity, only the elements present in the substrate, diffusion barrier and Mo contact are shown. The EDS line scan region is shown in the image; c) EDS line scan in the ACIGS layer, where the corresponding elements together with Fe are shown; d) Room

temperature TRPL decay for EBL-SLG, NIL-SLG and Flexible. A double exponential decays is observed for all substrates.

In order to study the mechanical stability of Flexible device (Figure 8a)), we calculated the applied strain, ε, on the device surface as it allows for the description of the physical device deformation during the bending[60,61]:

$$\varepsilon = \frac{t}{2R} \quad (1)$$

where, $t$ is the total thickness of the device, being 114 µm (substrate included) and $R$ the bending radius,14.4 mm. Thus, a strain of 0.4 % is induced in the devices when bent. Figure 8b) shows almost no variation in the $V_{OC}$ and $J_{SC}$ values throughout the bending tests, indicating: i) the mechanical strain did not led to a change in the ACIGS lattice; and ii) the optical properties were unaffected by mechanical deformation. However, the FF and efficiency values decreased in the first 50 bending cycles, while stabilising for the subsequent bending cycles. Studies show that FF might decrease in solar cells during bending measurements due to a deterioration in the window layer properties[62–64]. In fact, the ZnO based window layer used in our device is compatible with previously reported poor mechanical stability, since only a few bending cycles are needed to break down the material properties[62,63]. Therefore, for our flexible substrate, the window layer might be the cause for the decrease in the FF value and subsequently, the efficiency value. For flexible applications, where mechanical stability is of utmost importance, a different TCO should be used, such as Ag nanowires together with thin AZO, which demonstrated higher mechanical stability compared to standard TCO layers[64,65]. Nonetheless, the stable $V_{OC}$ and $J_{SC}$ indicates the excellent mechanical robustness of the electrical and optical properties of ultrathin CIGS based layer on stainless-steel substrates. The use of ultrathin absorber is advised for flexible applications, rather than conventional thin ones, where the absorber material might be four times thicker. This occurs due to a lower overall device thickness, which leads to a decrease in the applied strain. Thus, it can withstand a higher number of bending cycles without performance loss[58]. The solar cell results of Flexible and NIL-SLG show that NIL can pattern devices with efficiency values close to the well-established EBL process. The results of the Flexible device indicate that with the correct patterning technique, together with an optimized growth process, ultrathin flexible devices may reach the performance of rigid substrates.

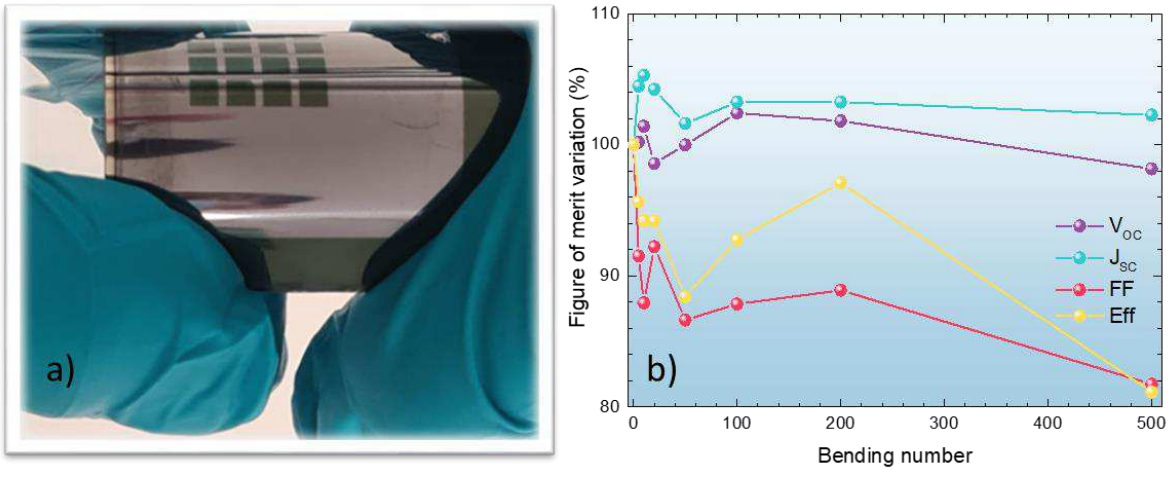

Figure 8 - a) Photography of the bent Flexible device; b) Flexible figures of merit variation as a function of the bending cycles.

## Conclusions

The pathway for the development of high-performance ultrathin flexible solar cells was established in this work, as ultrathin devices need the incorporation of a patterned passivation layer, we presented that NIL processing is fit for both patterning the necessary structure and that flexible substratesprossessing. Firstly, the NIL process was compared to a well-established lithography approach, EBL, in rigid substrates, followed by the patterning of a large area flexible substrate (15x15 $cm^2$). SEM and AFM analyses demonstrated the NIL uniformity on a 200 mm wafer and over a area of 15 x 15 $cm^2$, as well as the reproducibility between lithographic processes. Rigid devices demonstrated similar performances. Despite the similar TRPL decay lifetimes and $V_{OC}$ values, the EBL patterned device showed a higher $J_{SC}$ value, and a roll-over effect leading to a lower FF, compared to the NIL patterned device. XPS survey measurements showed the presence of F in Mo substrates etched by $C_4F_8$ based chemistry, being this element a by-product of the etch procedure used in the EBL device. The measured J-V curves were fitted with SCAPS, revealing different levels of compensation in the ACIGS layer, and $R_S$ and SRV values. These variations might be explained by the presence of F in the EBL device substrate, highlighting that the etch process of the patterning might be important for device performance. Furthermore, similar rear contact barrier values were obtained for both devices, therefore the roll-over effect was linked to charge accumulation, brought by the lower contacting area and h-SRV value for the EBL device. Nonetheless, the complexity of the simulated architectures along with the 1D nature of the simulation software might not be sufficient to explain the fit parameters through a one-diode model vision and more studies of the rear interface recombination are generally needed. The flexible device had a power conversion efficiency value of 11.7 %, slightly lower, albeit not a significant performance decrease, compared to the rigid devices. The flexible stainless-steel performance reflects the high ACIGS growth temperature, which might have promoted the diffusion of detrimental elements towards the absorber, which could also explain the TRPL sharper decay for the flexible device as opposed to the rigid ones. If present, Fe, is at a concentration too low to be clearly identified with STEM-EDS. However, the ACIGS absorber is extremely sensitive to Fe impurities and as such future works should work in understanding if there is really Fe diffusing and in alternative approaches to mitigate said diffusion. The high steel surface roughness values usually leads to lower FF values, in accordance to what was observed in this work. The flexible device showed excellent mechanical properties as the performance after 500 bending cycles showed only an 18 % variation to before bending and this degradation being likely linked to the TCO layer. As such, future studies of flexible substrates should be focused on improving diffusion barriers, processing, lowering roughness and making the TCO layer less prone to mechanical damage. All in all, we showed the successful implementation of rear passivation strategies in a lightweight large area flexible device, which is critical to the development of the CIGS technology in non traditional PV markets.

## Acknowledgements

This work was funded in part by the Fundação para a Ciência e a Tecnologia (FCT) under Grants 2020.04564.BD, IF/00133/2015, PD/BD/142780/2018, SFRH/BD/146776/2019, UIDB/04564/2020 and UIDP/04564/2020, 2020.07073.BD, as well as through the projects NovaCell (PTDC/CTM-CTM/28075/2017), CASOLEM (028917) “Correlated Analysis of Inorganic Solar Cells in and outside an Electron Microscope”, and InovSolarCells (PTDC/FISMAC/29696/2017) co-funded by FCT and the ERDF through COMPETE2020. And by the European Union's Horizon 2020 research and innovation

programme under the grants agreements N°. 720887 (ARCIGS-M project) and grand agreement N°.715027 (Uniting PV). The Special Research Fund (BOF) of Hasselt University is also acknowledged. P. Salomé and P. A. Fernandes would like to acknowledge FCT for the support of the project FCT UIDB/04730/2020. This work was developed within the scope of the project i3N, UIDB/50025/2020 & UIDP/50025/2020, financed by national funds through the FCT/MEC. The authors also acknowledge the support of Carlos Calaza in the fabrication for the 200 mm Si point contact stamp.

## Author Contributions

T. S. Lopes, J. P. Teixeira and P. M. P. Salomé conceived, designed and supervised the research. Electron beam lithography was performed by J. Borme. P. C. Sousa provided assistance for the 200 mm stamp fabrication. J. Ring and Y. Zhou provided assistance in the NIL process. SEM measurements were performed by K. Oliveira. AFM analysis was performed by B. R. Ferreira. Electrical measurements were performed and analysed by M. A. Curado, J. V. M. Cunha, and J. R. S. Barbosa. Data interpretation of TRPL was done by M. A. Curado and J. P. Teixeira. SCAPS simulations were performed by A. Violas and A. J. N. Oliveira. TEM measurements, analysis and sample preparation were performed by M. Monteiro, I. Çahan and L. Deepak. Bending measurements were performed and analysed by B. R. Ferreira. CIGS absorber layer growth and subsequent layers were performed by W. C. Chen and M. Edoff. Flexible substrates and assistance in flexible processing were provided by K. Takkei and E. Niemi. G. Brammertz, P. A. Fernandes, B. Vermang and P. M. P. Salomé secured funding. All authors contributed to the final version of manuscript. The manuscript was written by T. S. Lopes, J. P. Teixeira and P. M. P. Salomé and they also coordinated co-authors inputs, reviews and suggestions.

## Data Availability

The manuscript data that support the findings of this study are available from the corresponding authors upon reasonable request.

## Competing Interests

The authors declare no competing interests

## References

1. Ise, Fraunhofer Institute for Solar Energy Systems. *Photovoltaics Report*. 50 (2020).
2. Ramanujam, J. *et al.* Flexible CIGS, CdTe and a-Si:H based thin film solar cells: A review. *Progress in Materials Science* **110**, 100619 (2020).

3. Feurer, T. *et al.* Progress in thin film CIGS photovoltaics – Research and development, manufacturing, and applications. *Progress in Photovoltaics: Research and Applications* **25**, 645–667 (2017).
4. Kessler, F. & Rudmann, D. Technological aspects of flexible CIGS solar cells and modules. *Solar Energy* **77**, 685–695 (2004).
5. Reinhard, P. *et al.* Review of Progress Toward 20% Efficiency Flexible CIGS Solar Cells and Manufacturing Issues of Solar Modules. *IEEE Journal of Photovoltaics* **3**, 572–580 (2013).
6. Miasolé hits 20.56% efficiency with flexible CIGS technology. *pv magazine International* https://www.pv-magazine.com/2019/07/23/miasole-hits-20-56-efficiency-with-flexible-cigs-technology/.
7. Gloeckler, M. & Sites, J. R. Potential of submicrometer thickness Cu(In,Ga)$Se_2$ solar cells. *Journal of Applied Physics* **98**, 103703 (2005).
8. Amin, N., Chelvanathan, P., Hossain, M. I. & Sopian, K. Numerical Modelling of Ultra Thin Cu(In,Ga)Se2 Solar Cells. *Energy Procedia* **15**, 291–298 (2012).
9. Han, A. *et al.* Structure, morphology and properties of thinned Cu(In, Ga)$Se_2$ films and solar cells. *Semicond. Sci. Technol.* **27**, 035022 (2012).
10. Cunha, J. M. V. *et al.* Decoupling of Optical and Electrical Properties of Rear Contact CIGS Solar Cells. *IEEE J. Photovoltaics* **9**, 1857–1862 (2019).
11. Bose, S. *et al.* Optical Lithography Patterning of $SiO_2$ Layers for Interface Passivation of Thin Film Solar Cells. *Sol. RRL* **2**, 1800212 (2018).
12. Salomé, P. M. P. *et al.* Passivation of Interfaces in Thin Film Solar Cells: Understanding the Effects of a Nanostructured Rear Point Contact Layer. *Adv. Mater. Interfaces* **5**, 1701101 (2018).
13. Cunha, J. M. V. *et al.* High-Performance and Industrially Viable Nanostructured SiOx Layers for Interface Passivation in Thin Film Solar Cells. *Solar RRL* **5**, 2000534 (2021).
14. Lontchi, J. *et al.* Optimization of Back Contact Grid Size in $Al_2O_3$-Rear-Passivated Ultrathin CIGS PV Cells by 2-D Simulations. *IEEE Journal of Photovoltaics* **10**, 1908–1917 (2020).

15. Bose, S. *et al.* A morphological and electronic study of ultrathin rear passivated Cu(In,Ga)$Se_2$ solar cells. *Thin Solid Films* **671**, 77–84 (2019).
16. Schift, H. Nanoimprint lithography: An old story in modern times? A review. *J. Vac. Sci. Technol. B* **26**, 458 (2008).
17. Chou, S. Y., Krauss, P. R. & Renstrom, P. J. Imprint of sub-25 nm vias and trenches in polymers. *Appl. Phys. Lett.* **67**, 3114–3116 (1995).
18. Zhou, W. *et al.* Enhanced efficiency of light emitting diodes with a nano-patterned gallium nitride surface realized by soft UV nanoimprint lithography. *Nanotechnology* **21**, 205304 (2010).
19. Liu, Y. *et al.* The construction of Si2Sb2Te5electrical probe storage based on UV nanoimprint lithography. *Nanotechnology* **20**, 315304 (2009).
20. Ahn, S. H. & Guo, L. J. Large-Area Roll-to-Roll and Roll-to-Plate Nanoimprint Lithography: A Step toward High-Throughput Application of Continuous Nanoimprinting. *ACS Nano* **3**, 2304–2310 (2009).
21. Park, S. K. *et al.* Electrical characteristics of poly (3-hexylthiophene) thin film transistors printed and spin-coated on plastic substrates. *Synthetic Metals* **139**, 377–384 (2003).
22. Chang, J.-F. *et al.* Enhanced Mobility of Poly(3-hexylthiophene) Transistors by Spin-Coating from High-Boiling-Point Solvents. *Chem. Mater.* **16**, 4772–4776 (2004).
23. Bhingardive, V., Menahem, L. & Schvartzman, M. Soft thermal nanoimprint lithography using a nanocomposite mold. *Nano Res.* **11**, 2705–2714 (2018).
24. Ju, S. *et al.* Fabrication of perovskite solar cell with high short-circuit current density (JSC) using moth-eye structure of SiOX. *Nano Res.* **13**, 1156–1161 (2020).
25. Wang, C. *et al.* Discretely-supported nanoimprint lithography for patterning the high-spatial-frequency stepped surface. *Nano Res.* **14**, 2606–2612 (2021).
26. Essig, S., Paetel, S., Friedlmeier, T. M. & Powalla, M. Challenges in the deposition of (Ag,Cu)(In,Ga)Se $_2$ absorber layers for thin-film solar cells. *J. Phys. Mater.* **4**, 024003 (2021).

27. Edoff, M. *et al.* High $V_{oc}$ in (Cu,Ag)(In,Ga)$Se_2$ Solar Cells. *IEEE J. Photovoltaics* **7**, 1789–1794 (2017).

28. Yang, S.-C. *et al.* Silver-Promoted High-Performance (Ag,Cu)(In,Ga)$Se_2$ Thin-Film Solar Cells Grown at Very Low Temperature. *Solar RRL* **5**, 2100108 (2021).

29. Lopes, T. S. *et al.* Rear Optical Reflection and Passivation Using a Nanopatterned Metal/Dielectric Structure in Thin-Film Solar Cells. *IEEE J. Photovoltaics* **9**, 1421–1427 (2019).

30. Oliveira, K. *et al.* $SiO_x$ Patterned Based Substrates Implemented in Cu(In,Ga)$Se_2$ Ultrathin Solar Cells: Optimum Thickness. *IEEE Journal of Photovoltaics* 1–8 (2022) doi:10.1109/JPHOTOV.2022.3165764.

31. Cunha, J. M. V. *et al.* Insulator Materials for Interface Passivation of Cu(In,Ga)$Se_2$ Thin Films. *IEEE Journal of Photovoltaics* **8**, 1313–1319 (2018).

32. Yanaka, M., Tsukahara, Y., Nakaso, N. & Yanaka, M. Cracking phenomena of brittle films in nanostructure composites analysed by a modified shear lag model with residual strain. *Journal of Materials Science* **33**, 2111–2119 (1998).

33. Eriksson, T., Yamada, S., Venkatesh Krishnan, P., Ramasamy, S. & Heidari, B. High volume nanoimprint lithography on III/V substrates: Imprint fidelity and stamp lifetime. *Microelectronic Engineering* **88**, 293–299 (2011).

34. Graczyk, M. *et al.* Nanoimprint stamps with ultra-high resolution: Optimal fabrication techniques. *Microelectronic Engineering* **190**, 73–78 (2018).

35. Llobet, J. *et al.* Automated characterisation and analysis of large arrays of nanostructures fabricated at wafer scale. *Precision Engineering* **60**, 320–325 (2019).

36. Lindahl, J. *et al.* Inline Cu(In,Ga)$Se_2$ Co-evaporation for High-Efficiency Solar Cells and Modules. *IEEE Journal of Photovoltaics* **3**, 1100–1105 (2013).

37. Violas, A. F. *et al.* Will ultrathin CIGS solar cells overtake the champion thin-film cells? Updated SCAPS baseline models reveal main differences between ultrathin and standard CIGS. *Solar Energy Materials and Solar Cells* **243**, 111792 (2022).

38. Oliveira, A. J. N. *et al.* Encapsulation of Nanostructures in a Dielectric Matrix Providing Optical Enhancement in Ultrathin Solar Cells. *Solar RRL* **4**, 2000310 (2020).

39. de Wild, J. *et al.* High Voc upon KF Post-Deposition Treatment for Ultrathin Single-Stage Coevaporated Cu(In, Ga)$Se_2$ Solar Cells. *ACS Appl. Energy Mater.* **2**, 6102–6111 (2019).

40. Salomé, P. M. P., Rodriguez-Alvarez, H. & Sadewasser, S. Incorporation of alkali metals in chalcogenide solar cells. *Solar Energy Materials and Solar Cells* **143**, 9–20 (2015).

41. Umehara, T., Nakada, K. & Yamada, A. Impact of roll-over-shaped current–voltage characteristics and device properties of Ag(In,Ga)Se2 solar cells. *Jpn. J. Appl. Phys.* **56**, 012302 (2016).

42. Salomé, P., Fjällström, V., Hultqvist, A. & Edoff, M. Na Doping of CIGS Solar Cells Using Low Sodium-Doped Mo Layer. *IEEE Journal of Photovoltaics* **3**, 509–513 (2013).

43. Mansfield, L. M. *et al.* Efficiency increased to 15.2% for ultra-thin Cu(In,Ga)$Se_2$ solar cells. *Progress in Photovoltaics: Research and Applications* **26**, 949–954 (2018).

44. Yang, S. *et al.* Bandgap optimization of submicron-thick Cu(In,Ga)$Se_2$ solar cells. *Progress in Photovoltaics: Research and Applications* **23**, 1157–1163 (2015).

45. Nakamura, M. *et al.* Cd-Free Cu(In,Ga)$(Se,S)_2$ Thin-Film Solar Cell With Record Efficiency of 23.35%. *IEEE Journal of Photovoltaics* **9**, 1863–1867 (2019).

46. Oliveira, A. J. N. *et al.* Optoelectronic simulations for novel light management concepts in Cu(In,Ga)$Se_2$ solar cells. in *Physics, Simulation, and Photonic Engineering of Photovoltaic Devices X* vol. 11681 8–27 (SPIE, 2021).

47. Oliveira, A. J. N., Teixeira, J. P., Ramos, D., Fernandes, P. A. & Salomé, P. M. P. Exploiting the Optical Limits of Thin-Film Solar Cells: A Review on Light Management Strategies in Cu(In,Ga)Se2. *Advanced Photonics Research* **3**, 2100190 (2022).

48. Salomé, P. M. P. *et al.* Incorporation of Na in Cu(In,Ga)$Se_2$ Thin-Film Solar Cells: A Statistical Comparison Between Na From Soda-Lime Glass and From a Precursor Layer of NaF. *IEEE Journal of Photovoltaics* **4**, 1659–1664 (2014).

49. Salomé, P. M. P. *et al.* The effect of Mo back contact ageing on Cu(In,Ga)$Se_2$ thin-film solar cells. *Progress in Photovoltaics: Research and Applications* **22**, 83–89 (2014).

50. Vermang, B. *et al.* Introduction of Si PERC Rear Contacting Design to Boost Efficiency of Cu(In,Ga)$Se_2$ Solar Cells. *IEEE J. Photovoltaics* **4**, 1644–1649 (2014).

51. Vermang, B., Fjällström, V., Pettersson, J., Salomé, P. & Edoff, M. Development of rear surface passivated Cu(In,Ga)$Se_2$ thin film solar cells with nano-sized local rear point contacts. *Solar Energy Materials and Solar Cells* **117**, 505–511 (2013).

52. Rostan, P. J., Mattheis, J., Bilger, G., Rau, U. & Werner, J. H. Formation of transparent and ohmic ZnO:Al/MoSe2 contacts for bifacial Cu(In,Ga)$Se_2$ solar cells and tandem structures. *Thin Solid Films* **480–481**, 67–70 (2005).

53. Pianezzi, F. *et al.* Electronic properties of Cu(In,Ga)$Se_2$ solar cells on stainless steel foils without diffusion barrier. *Progress in Photovoltaics: Research and Applications* **20**, 253–259 (2012).

54. Wuerz, R., Eicke, A., Kessler, F. & Pianezzi, F. Influence of iron on the performance of CIGS thin-film solar cells. *Solar Energy Materials and Solar Cells* **130**, 107–117 (2014).

55. Pianezzi, F. *et al.* Influence of Ni and Cr impurities on the electronic properties of Cu(In,Ga)$Se_2$ thin film solar cells. *Progress in Photovoltaics: Research and Applications* **23**, 892–900 (2015).

56. Oueslati, S. *et al.* Study of $(Ag_xCu_{1-x})2ZnSn(S,Se)_4$ monograins synthesized by molten salt method for solar cell applications. *Solar Energy* **198**, 586–595 (2020).

57. Gessert, T. A. *et al.* Comparison of minority carrier lifetime measurements in superstrate and substrate CdTe PV devices. in *2011 37th IEEE Photovoltaic Specialists Conference* 001271–001274 (2011). doi:10.1109/PVSC.2011.6186189.

58. Curado, M. A. *et al.* Front passivation of Cu(In,Ga)$Se_2$ solar cells using $Al_2O_3$: Culprits and benefits. *Applied Materials Today* **21**, 100867 (2020).

59. Carron, R. *et al.* Advanced Alkali Treatments for High-Efficiency Cu(In,Ga)$Se_2$ Solar Cells on Flexible Substrates. *Advanced Energy Materials* **9**, 1900408 (2019).

60. Harris, K. D., Elias, A. L. & Chung, H.-J. Flexible electronics under strain: a review of mechanical characterization and durability enhancement strategies. *J Mater Sci* **51**, 2771–2805 (2016).
61. Mao, L., Meng, Q., Ahmad, A. & Wei, Z. Mechanical Analyses and Structural Design Requirements for Flexible Energy Storage Devices. *Advanced Energy Materials* **7**, 1700535 (2017).
62. Gerthoffer, A. *et al.* CIGS solar cells on flexible ultra-thin glass substrates: Characterization and bending test. *Thin Solid Films* **592**, 99–104 (2015).
63. Rathore, S. & Singh, A. Bending fatigue damage reduction in indium tin oxide (ITO) by polyimide and ethylene vinyl acetate encapsulation for flexible solar cells. *Eng. Res. Express* **2**, 015022 (2020).
64. Pandey, M. *et al.* Dependence of ITO-Coated Flexible Substrates in the Performance and Bending Durability of Perovskite Solar Cells. *Advanced Engineering Materials* **21**, 1900288 (2019).
65. Peng, C.-Y. *et al.* Strained Growth of Aluminum-Doped Zinc Oxide on Flexible Glass Substrate and Degradation Studies Under Cyclic Bending Conditions. *IEEE Trans. Device Mater. Relib.* **14**, 121–126 (2014).
66. Peng, C.-Y., Hamasha, M. M., VanHart, D., Lu, S. & Westgate, C. R. Electrical and Optical Degradation Studies on AZO Thin Films Under Cyclic Bending Conditions. *IEEE Trans. Device Mater. Relib.* **13**, 236–244 (2013).
67. Tsai, W.-C. *et al.* Flexible high performance hybrid AZO/Ag-nanowire/AZO sandwich structured transparent conductors for flexible Cu(In,Ga)$Se_2$ solar cell applications. *Journal of Materials Chemistry A* **4**, 6980–6988 (2016).
68. Liu, Y. *et al.* Draw-spun, photonically annealed Ag fibers as alternative electrodes for flexible CIGS solar cells. *Science and Technology of Advanced Materials* **20**, 26–34 (2019).

# Figure Legends

Figure 3 - Schematic representation of the lithography processes for patterning SLG based substrates with NIL (left) and EBL (right). Not at scale.

Figure 4 - Schematic with the 200 mm point contact Si Stamp fabrication steps. Not at scale.

Figure 3 - Top-view SEM images of: a) NIL-SLG and b) EBL-SLG substrates. The SEM images were taken with a Horizon field width (HFW) of 5 µm and an acceleration voltage of 5 kV. AFM cross-section profiles of a representative point contact of: c) NIL-SLG and d) EBL-SLG substrates obtained with a scan rate of 0.5 Hz. We note that the AFM obtained distance for both substrates is within average values for the SEM measurements.

Figure 4 - Top view SEM images of the 200 mm point contact stamp a) after the NIL process, b) after the Si etching, and c) After the resist removal and wafer cleaning. d) AFM cross-section profile of one point contact of the Si stamp.

Figure 5 - Top view SEM images after the resist removal, at opposite sides of flexible substrate, with the identification on the location of the SEM images. The point contact shape and dimension are retained regardless of the distance between the measurement, which indicates high quality for the demoulding step.

Figure 6 - a) Representative illuminated J-V curves; b) The figures of merit average and standard deviation values for the fabricated devices and in dark blue the ones obtained via SCAPS fit for EBL-SLG and NIL-SLG, additionally the rear barrier for holes, and the SRV for electrons and holes are also presented; c) Relative total diffuse reflection of Mo into a SLG and Stainless-steel substrate; d) XPS survey spectra of Mo based substrates without etch process, Mo_Ref, and with a BCl3 and C4F8 based etch process for substrate Mo_NIL and Mo_EBL, respectively are shown; e) SCAPS fit to the EBL-SLG and NIL-SLG illuminated J-V curves presented in a).

Figure 7 a) Cross section STEM image for Flexible device with the corresponding layers of the device identified; b) EDS line scan for the complete device. For clarity, only the elements present in the substrate, diffusion barrier and Mo contact are shown. The EDS line scan region is shown in the image; c) EDS line scan in the ACIGS layer, where the corresponding elements together with Fe are shown; d) Room temperature TRPL decay for EBL-SLG, NIL-SLG and Flexible. A double exponential decays is observed for all substrates.

Figure 8 - a) Photography of the bent Flexible device; b) Flexible figures of merit variation as a function of the bending cycles.

# Tables

Table 2 – Description of the samples' nomenclature, the thickness of the passivation layer, lithography used and the rear stack.

| Substrate/Device name | Lithography technique | Rear stack |
|---|---|---|
| EBL-SLG | EBL | SLG/Mo/$SiO_x$ |
| NIL-SLG | NIL | SLG/Mo/$SiO_x$ |
| Flexible | NIL | Steel/Mo/$SiO_x$ |